Vibration-induced field fluctuations in a superconducting magnet

J. W. Britton,[1,2,*] J. G. Bohnet,[1] B. C. Sawyer,[3] H. Uys,[4] M. J. Biercuk,[5] and J. J. Bollinger[1]

[1]*Time and Frequency Division, National Institute of Standards and Technology, Boulder, Colorado 80305, USA*
[2]*Army Research Lab, Adelphi, Maryland 20783, USA*
[3]*Georgia Tech Research Institute, Atlanta, Georgia 30332, USA*
[4]*Department of Physics, Stellenbosch University, 7600 Stellenbosch, South Africa and National Laser Centre,*
Council for Scientific and Industrial Research, Brummeria, 0184 Pretoria, South Africa
[5]*ARC Center for Engineered Quantum Systems, School of Physics, The University of Sydney, NSW 2006 Australia*
(Received 8 March 2016; published 27 June 2016)

Superconducting magnets enable precise control of nuclear and electron spins, and are used in experiments that explore biological and condensed-matter systems, and fundamental atomic particles. In high-precision applications, a common view is that slow (<1 Hz) drift of the homogeneous magnetic-field limits control and measurement precision. We report on previously undocumented higher-frequency field noise (10–200 Hz) that limits the coherence time of ^{9}Be$^+$ electron-spin qubits in the 4.46-T field of a superconducting magnet. We measure a spin-echo T_2 coherence time of $\sim$6 ms for the ^{9}Be$^+$ electron-spin resonance at 124 GHz, limited by part-per-billion fractional fluctuations in the magnet's homogeneous field. Vibration isolation of the magnet improved T_2 to $\sim$50 ms.

I. INTRODUCTION

In many spectroscopic applications the field stability of superconducing magnets is important. For example, in atomic physics superconducting magnets are used for high-precision mass spectroscopy [1–3] and stringent tests of quantum electrodynamics (QED) via magnetic moment measurements [4–7]. These many-hour experiments typically involve repeated quantum state preparation, evolution, and measurement. Slow drift of the homogeneous magnetic field is commonly believed to limit accurate comparison of sequential measurements.

A variety of techniques can improve long-term field stability to as low as 2×10^{-11}/h, enabling ion cyclotron mass spectroscopy at the $\sim 10^{-10}$ level [1] or better. One source of drift is the temperature-dependent susceptibility of in-bore materials [8,9]; controlling the liquid-cryogen boil-off rate (which varies with atmospheric pressure) and stabilization of the cryostat exterior temperature improves stability by reducing time variation of thermal gradients [1]. Sensitivity to ambient laboratory fields can be passively reduced by self-shielding [10] and by active feedback (to 10 Hz) [1,2]. Higher frequency fluctuations induced by vibrations and their mitigation are not well documented in the literature. Although high-field NMR installations ($>$500-MHz proton frequency) routinely employ vibration isolation [11,12], the fast part-per-billion noise we document here is beyond the detection capability of NMR, requiring high-frequency ESR (see Appendix 2).

II. APPARATUS

In the experiments described here, the homogeneous field of a superconducting magnet gives radial confinement of ^{9}Be$^+$ ions in a Penning trap, and defines the quantizing axis for the

^{9}Be$^+$ ions' valence-electron spin degree of freedom. Electron spin resonance (ESR) with these spins is sensitive to part-per-billion fractional field fluctuations at frequencies out to several hundred hertz (see the Appendix 2). Our measurements show correlations between the T_2 coherence of the electronic spin states with measured mechanical vibration of the magnet dewar. We further demonstrate that spin coherence may be extended by acoustic and vibration isolation of the magnet system.

Penning traps are routinely used in a wide range of studies including mass spectrometry of biological molecules (e.g., Fourier transform ion cyclotron resonance) [13] and tests of fundamental physics by precision spectroscopy (e.g., QED) [2,4–7]. Research aims of the NIST Penning trap include simulation of quantum magnetism [14] and potentially quantum computation [15,16]. Details of our setup have been described previously [14,17]. Here we summarize features important for measuring the magnetic-field noise and emphasize relevant system modifications since Ref. [17].

We confine a laser-cooled crystal of $N \sim 300$ ^{9}Be$^+$ ions in a Penning trap with a $B_0 = 4.46$-T superconducting magnet. Our two-level system (qubit) is the ^{9}Be$^+$ valence electron-spin states $|\uparrow\rangle \equiv |m_s = +1/2\rangle$ and $|\downarrow\rangle \equiv |m_s = -1/2\rangle$, where m_s is the spin's projection along the $B_0\hat{z}$ quantizing field. The spins' Larmor precession frequency Ω_0 is first-order field sensitive: $\hbar\Omega_0 \simeq g_J\mu_B B_0$, where $g_J \simeq -2.002$ is the electron g factor and μ_B is the Bohr magneton. Including a small hyperfine correction, $\Omega_o = 2\pi \times 124.05$ GHz for $B_0 = 4.46$ T. Similar to other nuclear magnetic resonance (NMR) and electron-spin resonance (ESR) experiments, arbitrary spin rotations are obtained with a resonant external microwave-frequency magnetic field $B_{\rm rf}\cos(\Omega_0 t)$. The microwave field is approximately uniform across all the ions and drives a spin flip $\tau_\pi = 68$ μs.

The superconducting magnet used in these experiments is a room-temperature bore (12.7-cm diameter) Nalorac Cryogenics Corporation [18] model 4.5/125 manufactured in 1990 [18]. The $\sim$50-cm tall NbTi superconducting solenoid

*joe.britton@gmail.com

produces a 4.5-T field for a continuous current of 58 A. Normal Z_0, Z_1, and Z_2 shim coils are wound on the room-temperature bore tube. The main superconducting coil and eight superconducting shim coils are fully immersed in a reservoir of liquid helium; the liquid-helium boil-off rate is 20 mL/h. A liquid-nitrogen sheath bears the brunt of the thermal load not deflected by layers of superinsulation. Nested vessels containing the liquid cryogens hang from attachment points within the cryogen-fill towers. Dielectric struts near the bottom of the dewar hold vessels apart and presumably provide some degree of mechanical damping. The dewar is constructed almost entirely of aluminum. The magnet's circulating supercurrent was stable from 2004 to 2013 and 2014 to present. The vacuum envelope of the Penning trap is rigidly attached to the magnet dewar.

III. MEASUREMENTS

In 2010 we noticed a correlation between mechanical vibration of laboratory floor and the potential across our magnet's normal-current in-bore Z_0 shim coil $V_{\text{emf}}(t)$. For the ambient laboratory environment, Figs. 1(a)–1(c) show V_{emf} as a voltage spectral density (S_V, $V/\sqrt{s^{-1}}$) and Fig. 1(c) shows the vibration measured as an acceleration spectral density (S_g, $g/\sqrt{s^{-1}}$). Acoustics also contribute to V_{emf}. The fundamental for a hollow pipe is $f_{\text{open}} = v(2L + 1.6d)^{-1} = 155$ Hz, where $v = 343$ m/s is the velocity of sound in air, and for our magnet bore, $L = 1$ m and $d = 0.127$ m. With an open magnet bore we see a broad spectral feature at $\sim$150 Hz that is strongly attenuated when the bore is covered by a laboratory notebook [Fig. 1(b)]. Mechanical resonances in the dewar likely contribute to V_{emf} as well. To explore this we induced mechanical motion of the magnet along the solenoid axis by applying a coherent driving force at frequency $\omega/2\pi$ to the top of the magnet dewar using an electromechanical oscillator (EMO) rigidly mounted to the top of the dewar. The EMO is a speaker solenoid (no diaphragm) driven by a sinusoid. We use lock-in detection to measure $V_{\text{emf}}(\omega)$ induced by the EMO drive. Resonances are observed in the frequency range of interest [Fig. 1(d)] but not all features in S_V can be explained in terms of resonances. Despite this complexity, we anticipated that S_V could be indicative of magnet-field fluctuations and T_2 coherence.

We measure the T_2 coherence of our spins using a spin-echo sequence illustrated in Fig. 2 with a single π pulse ($m = 2$). Optical pumping to $|\uparrow\rangle$ followed by a $\pi/2$ pulse rotates the spins to the equatorial plane of the Bloch sphere, defined to be the $\hat{y}$ axis in the rotating frame of the applied microwaves. At the end of the spin-echo evolution interval 2τ, we apply a final $\pi/2$ pulse with a phase shift θ relative the initial $\pi/2$ pulse, and then make a projective measurement of the z component of the spins (see the Appendix 1). For a given θ we repeat this experiment many times. From the phase and contrast of the resulting fringe pattern (obtained by varying θ), we measure that on average the spins maintain their alignment with the $\hat{y}$ axis but with reduced coherence $\langle \vec{\sigma}(2\tau) \rangle = \langle \hat{\sigma}_y(2\tau) \rangle$. T_2 corresponds to $T_2 = 2\tau$ when $\langle \hat{\sigma}_y(2\tau) \rangle = e^{-1}$. We note that our measurement of T_2 is sensitive to the phase evolution of the spins relative to the applied microwaves and is therefore
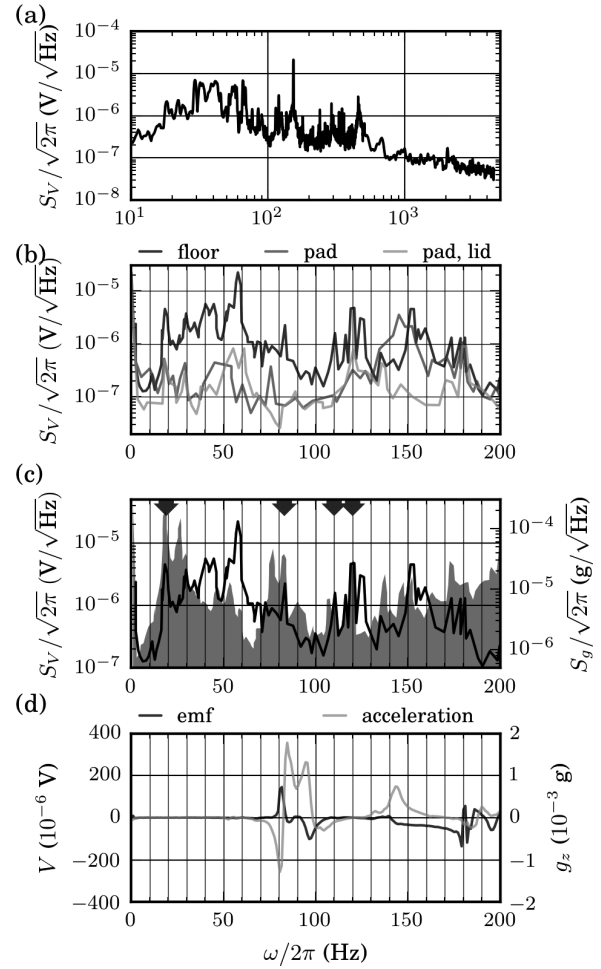

FIG. 1. An electromotive potential $V_{\text{emf}}(t)$ is induced on the magnet's normal Z_0 shim coil by fluctuating magnetic fields in the magnet bore. The voltage spectral density (S_V) of V_{emf} is plotted. (a) For $\omega/2\pi > 100$ Hz, S_V scales as ω^{-1} in this representative data from 2008 [19]. (b),(c) For the range $\omega/2\pi \lesssim 200$ Hz we observe that S_V is correlated with some (but not all) ambient seismic and acoustic noise in the laboratory. (b) S_V for the magnet coupled to the laboratory floor (black line). Several spectral features are suppressed by supporting the magnet on rubber vibration-isolation pads (dark gray line). The broad noise peak at 155 Hz is suppressed by covering the top side of the magnet bore with a laboratory notebook (light gray line). (c) The acceleration spectral density in the z direction (S_g, grey shaded area) and the S_V of V_{emf} (black line) are plotted for case of the magnet coupled to the laboratory floor. Correlations in the power spectra are marked with black arrows. (d) Lock-in detection at frequency $\omega/2\pi$ for signals V_{emf} (black line) and acceleration g_z (gray line) in response to a mechanical oscillator on top of the magnet dewar oscillating at frequency ω. A differential relationship is expected between V and g_z; a peak in the emf is expected at a zero crossing in g_z as at 83 Hz. The strongest correlation between resonant (d) and ambient (c) response is 83 Hz.

sensitive to magnetic-field fluctuations. This may be contrasted with many NMR and ESR experiments that determine the magnitude of the transverse spin coherence through measurement of both spin quadratures (see, for example, [20]). The spins' longitudinal relaxation T_1 is effectively infinite. We observed reduced T_2 under conditions when S_V is large (Fig. 3).
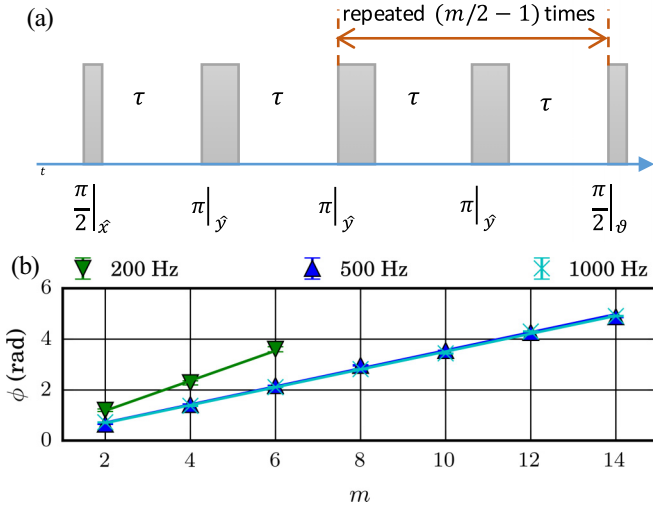
FIG. 2. (a) We measure the T_2 coherence of our spins using a spin-echo sequence ($m = 2$). The spin echo is first-order sensitive to coherent, synchronous field oscillations at frequency ω when $\tau = \frac{1}{2}(\omega/2\pi)^{-1}$. For $m = 2$ (interval 2τ) phase 2ϕ is acquired by the ion spins, where $\phi \propto \int_0^\tau B(t)dt$. (b) An independent calibration of the sensitivity of the Z_0 shim coil using m spin-echo sequences (see main text). We observe that $d\phi/dm$ is linear for EMF-induced magnetic fields at $\omega/2\pi = 200$ Hz, $\omega/2\pi = 500$ Hz, and $\omega/2\pi = 1000$ Hz.

Our key observations were consistently observed over an interval of five years in two different laboratory environments using two Penning traps. In 2011 [Fig. 3(a)] we observed an order of magnitude improvement in T_2 upon isolating the superconducting magnet, optics, and Penning trap from the laboratory floor using rubber flexural mounts (∼7 Hz resonant frequency, Barry Controls p/n 633A-260)[18]. Encouraged by this result, we moved our apparatus to a new laboratory space in 2014 which has lower ambient acoustic and seismic noise. In this new laboratory with the magnet coupled to the floor we observe increased T_2 [Fig. 3(b)] relative to the old laboratory

under the same conditions. In the new laboratory we isolated the magnet, trap, and optics from seismic vibration using pneumatic legs that support our optics table (∼1 Hz resonant frequency). The impact of magnet vibration isolation in both labs is an order of magnitude improvement in T_2 (Fig. 3). Despite the lower noise levels in the new laboratory, the T_2 observed with the magnet isolated is about the same as in the old laboratory. In the Appendixes 4–6 the potential sensitivity of T_2 to other factors is discussed including 124-GHz phase noise, magnetic-field gradients, and the presence of permeable materials in the magnet bore.

The observed increase in T_2 can be causally related to V_{emf} by noting that for a coil, a time-varying magnetic field $B(t) = B \sin(\omega t)$ induces a potential $V_{\text{emf}}(t) = V \cos(\omega t)$ with relative amplitude $V/B = \eta\omega$. Here, η is an unknown geometric factor with units of m^2. We assume that η is frequency invariant $S_B(\omega) = \frac{S_V(\omega)}{\eta\omega}$, where $S_B(\omega)$ is the magnetic-field spectral density in T/$\sqrt{\text{s}^{-1}}$. We use a filter function formalism to predict the spin coherence [19,21]. For a spin initially oriented along the y axis, its average projection along $\hat{y}$ after the interval 2τ is

$$\langle \sigma_y(2\tau) \rangle = e^{-\chi(2\tau)}, \tag{1}$$

where

$$\chi(2\tau) = \frac{1}{2\pi} \int_0^\infty S_\beta^2(\omega) F_1(\omega, 2\tau) \omega^{-2} d\omega. \tag{2}$$

Here, $S_\beta(\omega) = S_B(\omega) g \mu_B / \hbar$ is the spectral density of frequency fluctuations in units of s$^{-1}/\sqrt{\text{s}^{-1}}$ and $F_1(\omega, 2\tau) = 16 [\sin(\omega 2\tau/4)]^4$ is the spin-echo filter function in the limit of zero π-pulse length. This model is in qualitative agreement with observed decay of coherence in Fig. 3 taking η to be a free parameter. From these fits we obtain $\eta = 15$ m^2 (2011) and $\eta = 11$ m^2 (2014).

An independent calibration of η was obtained by coherent shaking of the magnet at ω using the EMO and observing $V_{\text{emf}}(\omega)$ and $B(\omega)$ using a spectrum analyzer and the ion spins respectively. The EMO-induced motion induces a magnetic
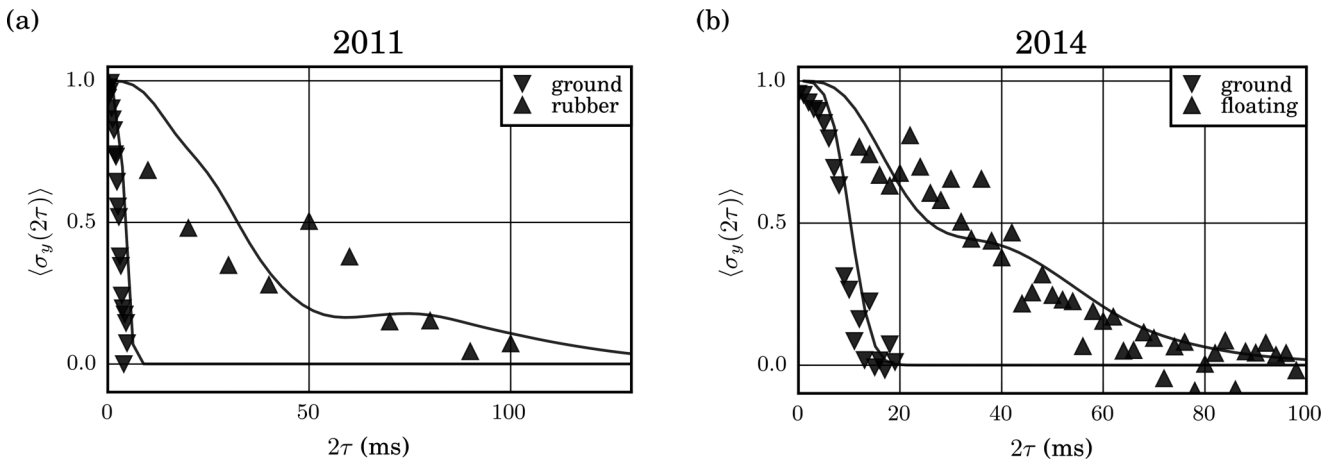

FIG. 3. Isolation of the magnet dewar from laboratory floor vibration increases T_2. (a),(b) Plots of spin Bloch vector length after a single π-pulse spin-echo experiment ($m = 2$) with total evolution time 2τ (points). Solid lines are theory curves given a magnetic-field noise spectrum inferred from V_{emf} with a single, frequency-independent η determined by best fit. (a) In 2011 we contrast T_2 when the magnet is in contact with floor vibration vs isolated by rubber isolation pads; a fit yields $\eta = 15$ m^2. (b) A similar experiment was performed in 2014 but with the magnet supported by a floating optics table; a fit yields $\eta = 11$ m^2.

field $B(t)$ that gives rise to a potential $V_0 \cos(\omega t)$ across the Z_0 shim coil, where $B(t) = V_0 \sin(\omega t)/\omega \eta$. Synchronous with the EMO drive, we perform a pulse sequence with $m - 1$ equally spaced π pulses and m intervals of duration $\tau = \frac{1}{2}(\omega/2\pi)^{-1}$. This sequence [Fig. 2(a)] is sensitive to a time-varying field at ω. For $m = 2$, during the interval 2τ a phase 2ϕ is acquired by the ion spins, where $\phi = \int_0^\tau \Delta(t) dt$ and $\Delta(t) = g\mu_B B(t)/\hbar$ is the shift in Larmor frequency due to $B(t)$. Each τ includes the 68-μs π-pulse time. The acquired phase ϕ is measured by varying the final $\pi/2$-pulse phase θ and extracting the phase of the resulting sinusoidal fringe pattern. A pulse sequence of length m yields phase accrual $m\phi$ [Fig. 2(b)]. From the slope $d\phi/dm$ and V_0, we calculate $\eta = 2g\mu_B V_0/(\hbar\omega^2 \frac{d\phi}{dm})$. This process was repeated for several EMO drive frequencies. For each ω the EMO drive phase was adjusted to maximize ϕ. We observed $\eta = 37$ m^2 at 200 Hz, $\eta = 7$ m^2 at 500 Hz and $\eta = 12$ m^2 at 1000 Hz. The dependence of η on frequency indicates that our assumption of frequency independence of η in the fits of Fig. 3 is simplistic. Nevertheless the mean values of η obtained from Fig. 3 and $d\phi/dm$ are similar. A better understanding of $\eta(\omega)$ is hampered by our poor knowledge of the exact geometry and mechanical support of the coils in our magnet.

The rms variation in the spin-flip frequency δ_{rms} due to S_B is

$$\delta_{\text{rms}}^2 = \frac{1}{\pi} \int_0^\infty S_\beta^2(\omega) d\omega \qquad (3)$$

(see the Appendix 3). Integrating S_β^2 for the conditions in Fig. 3 yields $\delta_{\text{rms}}/2\pi$ equal to 135 Hz (1.1 ppb) and 12 Hz (0.1 ppb) for the 2011 S_V data and 68 Hz (0.5 ppb) and 14 Hz (0.1 ppb) for the 2014 S_V data. We are not aware of other demonstrations of 0.1 ppb short-term stability in the electron spin-flip frequency in a high-field superconducting magnet.

IV. CONCLUSIONS

In summary, we observed part-per-billion fractional fluctuations in the homogeneous magnetic field of a 4.46-T superconducting magnet at frequencies up to 200 Hz. Using ^{9}Be$^+$ electron spins as sensitive field detectors, an order of magnitude reduction in integrated magnetic field noise was obtained by isolating the magnet from environmental acoustic and mechanical noise. Insomuch as our superconducting magnet is representative, we anticipate that a variety of high-precision measurements may be limited by similar fluctuations and could benefit from improved isolation. Examples include ESR and electron-cyclotron resonance with frequencies $\geqslant$90 GHz (see the Appendix 2) [4–7,22–24]. Fast field noise may underlie the 1×10^{-9} line-shape broadening observed but not well understood in single-electron g-factor experiments (5.4 T) [4,5] and in bound-electron magnetic-moment measurements of hydrogenic ^{28}Si^{13+} and ^{12}C^{5+} (3.8 T) [6,7]. High-frequency field fluctuations may also be important in high-field solid-state ESR experiments where some of the longest reported T2 coherence times are a few hundred microseconds (8.5 T) [23,24]. New materials with intrinsically longer spin-relaxation times are in development [25] and will require attention to field noise in the regime we discuss in this paper. The well-defined phase relationship between instantaneous V_{emf} and magnetic field suggests that

spin coherence could be further increased by feeding forward on the microwave phase.

APPENDIX

1. Penning trap

A Penning trap relies on static magnetic and electric fields to achieve three-dimensional confinement of ions. In equilibrium, the ion crystal rotates at angular frequency ω_r (about $\hat{z}$) and the Lorentz force ($q\vec{v} \times \vec{B}$) provides a radial restoring potential in the strong, homogeneous magnetic field $B_0\hat{z}$ (here, $B_0 = 4.46$ T). A static quadrupole electric potential gives axial trapping (along $\hat{z}$). The trap potential in a frame rotating at ω_r is

$$q\phi(r,z) = \frac{1}{2}M\omega_z^2(z^2 + \beta_r r^2), \qquad (A1)$$

where q is the ion charge, M is the single-ion mass, $\beta_r = \omega_r \omega_z^{-2}(\Omega_c - \omega_r) - 1/2$, Ω_c is the single-ion cyclotron frequency, and ω_z is ions' harmonic center-of-mass motion along $\hat{z}$. For ^{9}Be$^+$ ions in our trap potentials, $\Omega_c = B_0 q/M = 2\pi \times 7.6$ MHz and $\omega_z \sim 2\pi \times 800$ kHz. Ion rotation is precisely controlled with an external rotating quadrupole potential [26]. We set $\omega_r \sim 2\pi \times 45$ kHz so that the radial confinement is weak compared to the axial confinement ($\beta_r \ll 1$). Upon Doppler laser cooling the ions' motional degrees of freedom ($T \sim 1$ mK) [27], the ions naturally form a 2D Coulomb crystal consisting of one to four planes of ions. For $N \sim 300$ ions, the crystal diameter is $\leqslant$500 μm, and $\leqslant$60 μm along the magnetic field. The separation between planes is $\sim$20 μm.

Quantum control experiments begin with Doppler laser cooling followed by optical pumping to the $|\uparrow\rangle$ state using $\sim$313 nm laser light [17]. Projective readout of the ions' spin state is obtained by illuminating the ion crystal with a laser beam tuned to a cycling transition resonant with the $|\uparrow\rangle$ state and collecting fluorescence on a PMT; $|\uparrow\rangle$ ions appear bright, $|\downarrow\rangle$ ions appear dark. State preparation and detection requires 5 ms. Typical short-time Rabi flopping traces exhibit >99% contrast.

In the limit of large magnetic field, the ^{9}Be$^+$ nuclear spin is decoupled from the single valence electron. Optical pumping prepares the nuclear spin in the $|m_I = +3/2\rangle$ state.

2. Impact of magnetic field noise: ESR vs NMR

In high magnetic fields the impact of small, fast magnetic-field fluctuations is qualitatively different for ESR than for NMR and ion-cyclotron mass spectroscopy. Consider the case of a static magnetic field B_0 modulated at a single frequency ω_m with amplitude B_m,

$$B(t) = B_o + B_m \sin(\omega_m t). \qquad (A2)$$

TABLE I. Equation (A4) expresses the difference in sensitivity of NMR and ESR experiments. Suppose the field used in the present ESR experiment ($\Omega_0/2\pi = 124 \times 10^9$ Hz) was subject to ppb fractional fluctuations $\delta B/B_0 = 1 \times 10^{-9}$ at $\omega_m/2\pi = 50$ Hz. This corresponds to $\beta_m = 2.5$. For a nuclear spin (NMR) the equivalent modulation index is $\beta_m = 1 \times 10^{-3}$.

	β_m	J_0	J_1
ESR	2.5	-0.04	0.49
NMR	1×10^{-3}	1	7×10^{-4}

The instantaneous Larmor precession frequency is

$$\omega(t) = \Omega_o + \delta\omega_m \sin(\omega_m t), \qquad (A3)$$

where $\Omega_0 \equiv \gamma B_0$, where γ is the gyromagnetic ratio. The value of γ is $g_n\mu_N$ for a nuclear spin and $g_e\mu_B$ for an electron spin, where $g_e(g_n)$ is the electron (nuclear) g factor and $\mu_B(\mu_N)$ is the Bohr (nuclear) magneton. The frequency modulation of Eq. (A3) produces phase modulation of depth $\beta_m \equiv \delta\omega_m/\omega_m$ that results in sidebands at $\Omega_0 \pm n\omega_m$ of relative strength $J_n(\beta_m)$ and a depleted carrier of relative strength $J_0(\beta_m)$ where

$$\beta_m \equiv \frac{\delta\omega_m}{\omega_m} = \frac{\frac{B_m}{B_0}\Omega_0}{\omega_m} = \frac{B_m}{B_0}\frac{\Omega_0}{\omega_m}. \qquad (A4)$$

Since $J_0(\beta_m) \sim 1 - \frac{1}{4}\beta_m^2$, the carrier is substantially depleted for $\beta_m \sim 2$. Broadband noise also causes carrier attenuation.

The impact of Eq. (A2) on ESR and NMR is strikingly different (Table I). Suppose the field used in the present ESR experiment was subject to ppb fractional fluctuations $B_m/B_0 = 1 \times 10^{-9}$ at $\omega_m/2\pi = 50$ Hz on top of the homogeneous field B_0 responsible for the $\Omega_0/2\pi = 124 \times 10^9$ Hz Larmor precession (carrier). In this case, $\beta_m = 2.5$ and the carrier is fully depleted. In the case of a nuclear spin (NMR), the fractional sensitivity is reduced by $\sim\mu_B/\mu_N = 1836$ (μ_N is the nuclear magneton), $\beta_m = 1 \times 10^{-3}$, and the carrier suffers no depletion.

A complimentary analysis in the main text relates the power spectral density of frequency fluctuations $S_\beta^2(\omega)$ to the spin coherence [Eq. (2)]. The quadratic dependence of $S_\beta^2(\omega)$ on γ means decoherence is about a million times weaker for NMR than for ESR,

$$\chi_{\mathrm{NMR}}/\chi_{\mathrm{ESR}} = (\mu_N/\mu_B)^2 = 3 \times 10^{-7}.$$

That is, field noise that fully depletes (dephases) the Larmor carrier in the context of ESR has negligible impact on NMR.

3. rms magnetic field variation

We calculate the rms variation in spin-flip frequency δ_{rms} due to S_β as follows. Consider a Ramsey experiment with a free-evolution interval τ short enough that the spin-flip frequency remains constant over τ. Let δ be the instantaneous frequency deviation of the spin-flip frequency from its mean. The accumulated phase difference between the microwaves and the spins is then $\phi = \delta\tau$. In the limit $\delta_{\mathrm{rms}}\tau \ll 1$ and averaging over many experiment repetitions, the Bloch vector length is

$$\langle\hat{\sigma}_y\rangle = \langle\cos\phi\rangle \simeq 1 - \tfrac{1}{2}\delta_{\mathrm{rms}}^2\tau^2. \qquad (A5)$$

Applying the filter function formalism and expanding to first order,

$$e^{-\chi(\tau)} \simeq 1 - \chi(\tau) = 1 - \frac{1}{2\pi}\int_0^\infty S_\beta^2(\omega)F_0(\omega,\tau)\omega^{-2}d\omega$$

$$= 1 - \left\{\frac{1}{2\pi}\int_0^\infty S_\beta^2(\omega)d\omega\right\}\tau^2, \qquad (A6)$$

where $F_0(\omega,\tau) = 4\sin^2(\omega\tau/2)$ is the Ramsey filter function and we have used the small angle approximation. We then obtain

$$\delta_{\mathrm{rms}}^2 = \frac{1}{\pi}\int_0^\infty S_\beta^2(\omega)d\omega. \qquad (A7)$$

4. Microwave phase noise

Since microwave phase noise can also limit T_2, we use a low phase noise microwave synthesis chain. It starts with a low noise quartz oscillator at 100 MHz which is subsequently multiplied up to 124 GHz. Due to multiplication, the phase noise at 100 MHz is at least $20\log_{10}(1240)$ dB $= 62$ dB larger at 124 GHz. The ions are exposed to microwaves from outside the vacuum chamber by a $\sim$1-m long, open-ended WR-8 waveguide. Prior to 2011, we generated 124 GHz using a Gunn diode oscillator whose phase noise precluded T_2 measurements beyond $\sim$10 ms [17,28]. In 2011 the synthesis chain was upgraded as discussed in Fig. 4 and its phase noise is not expected to impact spin coherence for $2\tau < 1$ s.

5. Field gradients

Ion movement through a magnetic-field gradient can produce an apparent time dependence to the magnetic field. Here we discuss the potential sensitivity of our T_2 measurements to magnetic-field gradients.

Field gradients in our superconducting solenoid were minimized by applying currents to superconducting $(z, z^3, x, y, xz, yz, xy, x^2 - y^2)$ and normal (z, z^2) shim coils. Shimming the superconducting coils was performed using a deuterium oxide (D_2O) probe without the Penning trap inserted in the magnet bore. The field gradients in Table II were measured in 2014 using small crystals of ions as a field probe. The ions were translated in the axial (radial) direction by applying a bias to an endcap (rotating wall) electrode, and the resulting shift in electron spin-flip frequency was measured. The measured gradients are comparable to those observed in 2010 [17], except the linear axial gradient, which is significantly improved.

The gradients measured using the ions as field probe (Table II) are up to an order of magnitude larger than those observed using the D_2O probe and otherwise empty magnet bore. This indicates that parts of the Penning apparatus include permeable materials. Gradient compensation with the Penning trap in the bore is possible, but has not yet been attempted due to a non-negligible risk of magnet quench.

The ion crystal axial extent along $\hat{z}$ is sensitive to the z and z^2 terms. For four planes ($\sim$60 μm), the axial gradients produce a spread in the electron spin-flip frequency of $\sim$50 Hz. Ion crystal rotation averages the radial gradients to zero, except for the $x^2 + y^2$ term which can produce a $\sim$170-Hz dispersion in the electron spin-flip frequency for a 250-μm
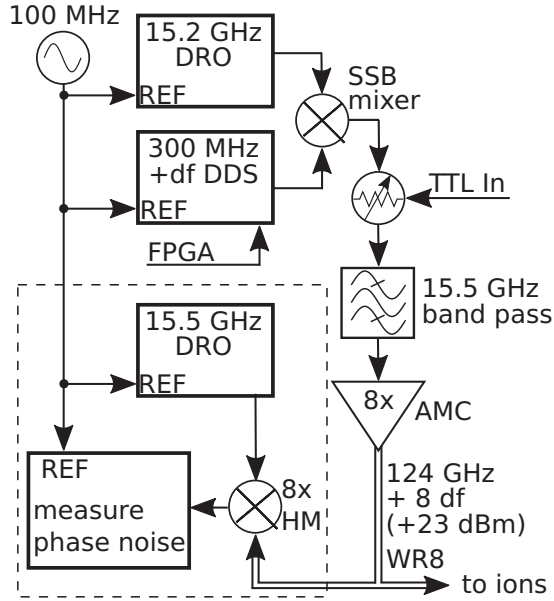
FIG. 4. Low phase noise synthesis chain for 124 GHz. The phase reference is a Spectra Dynamics Inc. [18] LNFR-100 low noise quartz oscillator at 100 MHz which is disciplined below 100 Hz by a low phase noise 5 MHz quartz oscillator. A 15.2-GHz DRO (Lucix Inc.) is phase locked to the LNFR-100. Frequency and phase agility is obtained by mixing the 15.2 GHz with a ~300-MHz tone derived from a FPGA-controlled direct digital synthesizer (DDS, Analog Devices AD9858) using a single-sideband (SSB) mixer (Polyphase Microwave). Fast switching is provided by a TTL-controlled absorptive switch (Hittite). The 15.5-GHz sideband is filtered by a 100-MHz passband cavity filter (Anatech Inc.) and fed to a nonresonant, free-running chain of room-temperature amplifiers and multipliers (AMC, Virginia Diode Inc.). The AMC produces ~200 mW at 124 GHz. The microwaves are transmitted to the ions in the magnet bore over a ~1-m WR8 waveguide. No horn is used; coupling to free space is with an open-ended WR8 waveguide. The phase noise at 124 GHz was measured (dashed box) on a bench top using a spectrum analyzer, 8x harmonic mixer (Millitech), and a 15.5-GHz reference DRO (Lucix Inc.). We observed -70 dBc at 200-Hz offset, -85 dBc from 1 to 10-kHz offsets, and -93 dBc at 100-kHz offset.

radius. The spin echo will cancel out the effect of these gradients as long as the ions do not move within the crystal. Although measurements of T_2 are performed with the cooling laser blocked, previous work showed that the period of time for a small crystal to melt is longer than 100 ms [29]. A further indication that ion movement within the crystal is not limiting our T_2 measurements is that their standard deviation is consistent with homogeneous dephasing.

Movement of the vacuum envelope and Penning trap electrodes within the magnet bore would result in a center-of-mass motion of the ion crystal. This would produce a homogeneous time dependence of the magnetic field sensed by the ions. High-resolution images of the ions place a limit on the amplitude of such motion to <3 μm. A 3-μm movement along the largest linear gradient ($dB/dy = 780\times10^{-6}$ T/m) generates a ~70-Hz change in the spin-flip frequency. Since we see much smaller spin-flip frequency fluctuations than

TABLE II. Magnetic-field inhomogeneity was quantified over a ~0.3-mm radius volume using the ions' electron spin flip as a field sensor (28 GHz/T). This region was sampled by applying static potentials to endcap (rotating wall) electrodes to induce axial (radial) displacements of the ion crystal. Room-temperature shim coils permit minimization of the axial field gradients.

	Gradients	10^{-6}
x	0.42	T/mm
y	0.78	T/mm
xy	<0.2	T/mm^2
$x^2 - y^2$	<0.2	T/mm^2
$x^2 + y^2$	<0.1	T/mm^2
z	<0.03	T/mm
z^2	<0.2	T/mm^2

70 Hz, we anticipate that movement of the vacuum envelope is much less than 3 μm. However, this effect may limit our T_2 coherence times with the magnet vibrationally isolated.

The x- and y-linear gradients in Table II appear to be due to permeable material placed in the magnet bore, and could be improved by reshimming the magnet with the superconducting shim coils while using the ions to sense the gradient.

6. Permeable materials in magnet bore

Permeable materials in the magnet bore give rise to additional magnetic fields and field gradients, and their mechanical motion and temperature variation causes time variation in the field sensed by the ions. The Penning trap itself is constructed from low permeability materials (type-2 titanium, Macor, aluminum, OFHC copper, Kapton, and fused silica), and the approximately cylindrical arrangement of these materials should minimize gradients. Also in the magnet bore are relatively large structures that guide laser beams and support photon collection optics. The structures are not mechanically tied directly to the Penning trap. Images of the ions constrain the axial $\hat{z}$ motion of the structures within the magnet bore to <3 μm.

The largest support structure is a 5-cm-long aluminum cylinder (12.5 cm OD, 7.5 cm ID). The magnetization of a permeable material is given by $M = \chi H = \chi B/\mu_0$; $\chi = 2.22\times10^{-5}$ for aluminum. The field produced by a uniform magnetization can be calculated by an equivalent current on the surface of the aluminum. The largest gradient is at the ends of the dewar where $\frac{dB_z}{dz} = 630\times10^{-6}$ T/m in the 4.5-T field of the magnet. The fractional magnetic-field variation due to a 3-μm displacement of the cylinder is $\frac{1}{B}\frac{dB}{dz}dz = 4.2\times10^{-10}$ (52 Hz). Field fluctuations at the location of the ions are expected to be smaller than this estimate by 20–30%.

The variation in the susceptibility of aluminum with temperature is not completely negligible. We estimate a dependence of the field sensed by the ions on the aluminum cylinder temperature to be $\frac{1}{B}\frac{dB}{dT} = 3\times10^{-9}/\,^\circ$C. Temperature changes will occur on time scales slower than those considered in these experiments.

We note that the V_{emf} induced in the room-temperature Z_0 shim coil was not significantly changed with the trap and supporting structures mounted in the magnet bore.

The considerations in this section indicate that the permeable materials inserted into the magnet bore did not significantly contribute to the T_2 measurements with the magnet sitting on the floor. However, this effect may contribute to T_2 coherence times with the magnet vibrationally isolated.

---

[1] R. S. Van Dyck, D. L. Farnham, S. L. Zafonte, and P. B. Schwinberg, Rev. Sci. Instrum. **70**, 1665 (1999).

[2] E. G. Myers, Int. J. Mass Spectrom. **349–350**, 107 (2013).

[3] S. Rainville, J. K. Thompson, and D. E. Pritchard, Science **303**, 334 (2004).

[4] B. Odom, D. Hanneke, B. D'Urso, and G. Gabrielse, Phys. Rev. Lett. **97**, 030801 (2006).

[5] D. Hanneke, S. Fogwell, and G. Gabrielse, Phys. Rev. Lett. **100**, 120801 (2008).

[6] S. Sturm, A. Wagner, B. Schabinger, J. Zatorski, Z. Harman, W. Quint, G. Werth, C. Keitel, and K. Blaum, Phys. Rev. Lett. **107**, 023002 (2011).

[7] S. Sturm, F. Köhler, J. Zatorski, A. Wagner, Z. Harman, G. Werth, W. Quint, C. H. Keitel, and K. Blaum, Nature (London) **506**, 467 (2014).

[8] G. L. Salinger and J. C. Wheatley, Rev. Sci. Instrum. **32**, 872 (1961).

[9] Z. Xia, J. Bray-Ali, J. Zhang, R. B. Fink, K. S. White, C. M. Gould, and H. M. Bozler, J. Low Temp. Phys. **126**, 655 (2002).

[10] G. Gabrielse and J. Tan, J. Appl. Phys. **63**, 5143 (1988).

[11] H. J. Schneider-Muntau, Solid State Nucl. Magn. Reson. **9**, 61 (1997).

[12] T. Kiyoshi, S. Choi, S. Matsumoto, K. Zaitsu, T. Hase, T. Miyazaki, A. Otsuka, M. Yoshikawa, M. Hamada, M. Hosono, Y. Yanagisawa, H. Nakagome, M. Takahashi, T. Yamazaki, and H. Maeda, IEEE Trans. Appl. Supercond. **20**, 714 (2010).

[13] A. G. Marshall, C. L. Hendrickson, and G. S. Jackson, Mass Spectrom. Rev. **17**, 1 (1998).

[14] J. W. Britton, B. C. Sawyer, A. C. Keith, C.-C. J. Wang, J. K. Freericks, H. Uys, M. J. Biercuk, and J. J. Bollinger, Nature (London) **484**, 489 (2012).

[15] D. Porras, J. I. Cirac, S. Kilina, S. Tretiak, and E. Einarsson, Phys. Rev. Lett. **96**, 250501 (2006).

[16] J. D. Baltrusch, A. Negretti, J. M. Taylor, and T. Calarco, Phys. Rev. A **83**, 042319 (2011).

[17] M. J. Biercuk, H. Uys, A. P. VanDevender, N. Shiga, W. M. Itano, and J. J. Bollinger, Quantum Inf. Comput. **9**, 920 (2009).

[18] NIST does not endorse commercial products. We provide reference to the suppliers of the specific instrumentation used in this work for informational purposes only.

[19] M. J. Biercuk, H. Uys, A. P. VanDevender, N. Shiga, W. M. Itano, and J. J. Bollinger, Nature (London) **458**, 996 (2009).

[20] G. W. Morley, L. Brunel, and J. van Tol, Rev. Sci. Instrum. **79**, 064703 (2008).

[21] M. J. Biercuk, A. C. Doherty, and H. Uys, J. Phys. B **44**, 154002 (2011).

[22] J. Ahokas, J. Järvinen, G. V. Shlyapnikov, and S. Vasiliev, Phys. Rev. Lett. **101**, 263003 (2008).

[23] S. Takahashi, R. Hanson, J. van Tol, M. Sherwin, and D. D. Awschalom, Phys. Rev. Lett. **101**, 047601 (2008).

[24] G. W. Morley, D. R. McCamey, H. A. Seipel, L.-C. Brunel, J. van Tol, and C. Boehme, Phys. Rev. Lett. **101**, 207602 (2008).

[25] A. M. Tyryshkin, S. Tojo, J. J. L. Morton, H. Riemann, N. V. Abrosimov, P. Becker, H.-J. Pohl, T. Schenkel, M. L. W. Thewalt, K. M. Itoh, and S. A. Lyon, Nat. Mater. **11**, 143 (2011).

[26] T. B. Mitchell, J. J. Bollinger, D. Dubin, X. Huang, W. M. Itano, and R. H. Baughman, Science **282**, 1290 (1998).

[27] B. C. Sawyer, J. W. Britton, A. C. Keith, C.-C. J. Wang, J. K. Freericks, H. Uys, M. J. Biercuk, and J. J. Bollinger, Phys. Rev. Lett. **108**, 213003 (2012).

[28] N. Shiga, W. M. Itano, and J. J. Bollinger, Phys. Rev. A **84**, 012510 (2011).

[29] M. J. Jensen, T. Hasegawa, and J. J. Bollinger, Phys. Rev. A **70**, 033401 (2004).